

Exploring Intrinsic Bond Orbitals in Solids

Benjamin Wöckinger, Alexander Rumpf, and Tobias Schäfer*

Institute for Theoretical Physics, TU Wien, Wiedner Hauptstraße 8-10/136, A-1040

Vienna, Austria

E-mail: tobias.schaefer@tuwien.ac.at

Abstract

We present a study of the construction and spatial properties of localized Wannier orbitals in large supercells of insulating solids using plane waves as the underlying basis. The Pipek-Mezey (PM) functional in combination with intrinsic atomic orbitals (IAOs) as projectors is employed, resulting in so-called intrinsic bond orbitals (IBOs). Independent of the bonding type and band gap, a correlation between orbital spreads and geometric properties is observed. As a result, comparable sparsity patterns of the Hartree-Fock exchange matrix are found across all considered bulk 3D materials, exhibiting covalent bonds, ionic bonds, and a mixture of both bonding types. Recognizing the considerable computational effort required to construct localized Wannier orbitals for large periodic simulation cells, we address the performance and scaling of different solvers for the localization problem. This includes the Broyden-Fletcher-Goldfarb-Shanno (BFGS), Conjugate-Gradient (CG), Steepest Ascent (SA) as well as the Direct Inversion in the Iterative Subspace (DIIS) method. Each algorithm performs a Riemannian optimization under unitary matrix constraint, efficiently reaching the optimum in the “curved parameter space” on geodesics. We hereby complement the literature with an introduction to this topic along with key references. Furthermore, we observe that the construction of Wannier orbitals for su-

percells of metal oxides presents a significant challenge, requiring approximately one order of magnitude more iteration steps than other systems studied.

1 Introduction

Localized orbitals are a useful tool in quantum chemistry and materials physics. They serve a variety of purposes, for example, the analysis of chemical bonds in tune with chemical intuition,^{1,2} the investigation of electron transfer processes,³ the calculation of electron-phonon interactions,⁴ or the development of efficient many-electron correlation algorithms with reduced computational cost.⁵⁻¹¹

Known as localized Wannier orbitals in solid-state physics and localized molecular orbitals in quantum chemistry, they are usually derived from delocalized one-electron mean-field orbitals through rotations, achieved by a unitary matrix, resulting in spatial confinement. Various definitions have been proposed for determining this unitary matrix,^{1,12-14} with several implementations available for periodic systems.^{9,15-20}

Here, we consider localized orbitals as a tool to introduce sparsity in Coulomb integrals, with the long-term goal of addressing the scaling problem in many-electron correlation methods. Our focus is on large simulation cells, which are essential for realistic models, for example, surface phenomena and defects. Consequently, we examine the scalability of constructing localized Wannier orbitals for large periodic cells of materials containing several hundred atoms. To this end we study the performance of various solvers. In addition to this technical investigation, we report an intriguing result that we found during our research: for all considered semiconductors the sparsity in the Fock exchange matrix is almost unaffected by the band gap of the material.

The paper is divided into two main parts, which follow after a brief theoretical summary of the definition of IBOs for solids and a description of the employed software packages and computational settings in Sec. 2. The first main part is in Sec. 3 where we discuss

the theory, implementation, and performance of different numerical solvers to numerically construct IBOs. This part also aims to complement the existing literature by providing a pedagogical mathematical introduction to the topic of Riemannian optimization under unitary matrix constrain, along with key references essential for those starting in this area. The second main part is in Sec. 4 where we report spatial properties of IBOs, an analysis of the sparsity of the Fock exchange matrix, and trends across the considered materials.

2 Computational Methods & Intrinsic Bond Orbitals

In solids, intrinsic bond orbitals (IBOs), $|\mathcal{W}_{\mathbf{R}j}\rangle$, can be defined as generalized Wannier orbitals.^{9,16} They are constructed as superpositions of Bloch orbitals, $|\chi_{j\mathbf{k}}\rangle$, obtained from prior mean-field calculations such as Hartree-Fock (HF) or Kohn-Sham density functional theory (DFT),

$$|\mathcal{W}_{\mathbf{R}j}\rangle = \frac{1}{V_{\text{BZ}}} \int_{\text{BZ}} d^3k e^{-i\mathbf{k}\mathbf{R}} \sum_i^{N_{\text{occ}}} u_{ij}^{(\mathbf{k})} |\chi_{j\mathbf{k}}\rangle. \quad (1)$$

Here, $u_{ij}^{(\mathbf{k})}$ is a unitary matrix at each \mathbf{k} -point \mathbf{k} , and V_{BZ} represents the volume of the Brillouin zone (BZ).

In this work, all calculations are based on HF orbitals obtained from the plane-wave based Vienna Ab initio Simulation Package (VASP).²¹⁻²³ Supercells are considered using a Γ -only sampling of the BZ, reducing Eq. (1) to

$$|\mathcal{W}_j\rangle = \sum_i^{N_{\text{occ}}} u_{ij} |\chi_j\rangle. \quad (2)$$

The matrix u_{ij} is optimized to maximize (minimize) a localization functional \mathcal{L} , which defines the localized Wannier orbitals. Various localization functionals exist in the literature, such as Foster-Boys (FB),¹² Edmiston-Ruedenberg (ER),¹ von-Niessen (VN),¹³ and Pipek-Mezey (PM).¹⁴ Our Riemannian optimization algorithm²⁴ described in Sec. 3.1.1 is suited for any cost functional, allowing us to compare the case of PM, FB, and VN. Since we employ

Γ -point-only sampling, the unitary matrices here are in fact real and orthogonal matrices.

Intrinsic bond orbitals were introduced by Knizia² and are the result of maximizing the PM functional,

$$\mathcal{L}^{\text{PM}}[\{u_{ij}\}] = \sum_i^{N_{\text{occ}}} \sum_A^{N_{\text{atoms}}} |\langle \mathcal{W}_i | \mathbf{P}_A | \mathcal{W}_i \rangle|^2, \quad (3)$$

where $\mathbf{P}_A = \sum_{\mu \in A} |\mu\rangle\langle\mu|$ are projectors onto a certain set of atom-centered functions $|\mu\rangle$, also known as intrinsic atomic orbitals (IAOs). This choice provides an unbiased measure of atomic partial charges and addresses the well-known basis set dependence associated with Mulliken populations. The IAOs can be constructed from any set of atomic functions $|f_\mu\rangle$ via the projection:

$$|\mu^{\text{IAO}}\rangle = (\mathbf{1} + \mathcal{O} - \tilde{\mathcal{O}})|f_\mu\rangle, \quad (4)$$

where \mathcal{O} is the projector onto the occupied space and $\tilde{\mathcal{O}}$ projects onto the space spanned by occupied orbitals from a minimal atomic basis. These projectors are defined as:

$$\mathcal{O} = \sum_i^{N_{\text{occ}}} |\chi_i\rangle\langle\chi_i|, \quad \tilde{\mathcal{O}} = \sum_i^{N_{\text{occ}}} |\tilde{\chi}_i\rangle\langle\tilde{\chi}_i|, \quad (5)$$

with the orbitals $|\tilde{\chi}_i\rangle$ given by

$$|\tilde{\chi}_i\rangle = \text{orth} \left[\sum_{\mu\nu} |f_\mu\rangle S_{\mu\nu}^{-1} \langle f_\nu | \chi_i \rangle \right], \quad (6)$$

where $S_{\mu\nu} = \langle f_\mu | f_\nu \rangle$ is the overlap matrix of the atomic functions. The "orth" denotes orthogonalization.

The orbitals $|\tilde{\chi}_i\rangle$ approximate the occupied orbitals in the minimal atomic basis $|f_\mu\rangle$, while the exact occupied mean-field orbitals $|\chi_i\rangle$ are obtained from a preceding mean-field calculation in the plane-wave basis, which is considered a complete basis. The term $\mathcal{O} - \tilde{\mathcal{O}}$ in Eq. (4) augments the atomic functions to form the IAOs, ensuring completeness of the occupied space. As long as no occupied orbital is orthogonal to the atomic functions, i.e., $\sum_\nu \langle f_\nu | \chi_i \rangle \neq 0, \forall i$, the IAOs form an exact atom-centered basis for the occupied space.

3 Construction of Intrinsic Bond Orbitals

Efficient optimization algorithms are vital for the success of localization methods, relying on the optimization of an orbital-dependent cost function \mathcal{L} . As described previously in Sec. 2, we employ the IBO method. Optimization is performed using a Riemannian geometry approach, exploiting the topological properties of the unitary group to preserve the unitary constraint inherently. The search directions are translated to geodesics on the manifold, leading to more efficient optimization steps. Early works on these topics were conducted, for example, by Luenberger and Gabay.^{25,26}

3.1 Riemannian optimization under unitary constraint

Riemannian optimization leverages the theory of optimization and concepts of differential geometry, more specifically Riemannian manifolds. We follow the works of Abrudan et al.^{27,28} and Huang et al.^{29,30}

3.1.1 Unconstrained Optimization

In this section, we introduce the concept of unconstrained line search algorithms, which are later adapted for application on manifolds. A minimum (or maximum) of some function $\mathcal{L}(\mathbf{U})$ is approached iteratively, where \mathbf{U} represents an abstract vector in the parameter space. The optimization algorithms we compare are Conjugate-Gradient (CG), limited-memory BFGS (L-BFGS) and Steepest Ascent (SA) solvers, in this paper we focus particularly on the first two, as SA has proven to be clearly inferior in our calculations and in Refs.^{18,20} Line search algorithms select a suitable direction in parameter space in a first step and subsequently determine an optimal step size along that chosen path. A detailed treatment of these topics can be found in Ref.³¹ Without constraints, these algorithms are unrestricted within the respective parameter space, and follow the general update formula

$$\mathbf{U}_{k+1} = \mathbf{U}_k + \alpha_k \mathbf{H}_k, \tag{7}$$

where the iterates \mathbf{U}_{k+1} and \mathbf{U}_k are estimates of the desired extremum, α_k is the step size \mathbf{H}_k is the search direction.

For SA, the search direction \mathbf{H} is chosen as the gradient $\nabla\mathcal{L}(\mathbf{U}_k)$. The CG search direction is calculated according to the formula:

$$\mathbf{H}_k = \nabla\mathcal{L}(\mathbf{U}_k) + \beta_k\mathbf{H}_{k-1}, \quad (8)$$

where β is a weighting factor that uses information from the previous step, we use the Polak-Ribière (PR) factor.^{32,33} The initial search direction is $H_0 = \nabla\mathcal{L}(\mathbf{U}_0)$. BFGS³⁴⁻³⁷ is a quasi-Newton algorithm that mimics Newton's method of minimizing the second-order Taylor series of the cost function. The Newton search direction is $\mathbf{H}_k = -\mathbf{B}_k\nabla\mathcal{L}(\mathbf{U}_k)$ with the inverse Hessian \mathbf{B}_k . For high-dimensional problems, the computational cost of calculating the Hessian or its inverse is usually prohibitively high, so quasi-Newton algorithms aim for an accurate approximation. The limited-memory BFGS (L-BFGS) approximation is given by:

$$\mathbf{B}_{k+1} = (\mathbf{I} - \rho_k\mathbf{y}_k\mathbf{s}_k^T)\mathbf{B}_k(\mathbf{I} - \rho_k\mathbf{y}_k\mathbf{s}_k^T) + \rho_k\mathbf{s}_k\mathbf{s}_k^T \quad (9)$$

where \mathbf{I} is the identity,

$$\rho_k = \frac{1}{\mathbf{y}_k^T\mathbf{s}_k}, \quad (10)$$

and

$$\mathbf{s}_k = \mathbf{U}_{k+1} - \mathbf{U}_k, \quad \mathbf{y}_k = \nabla\mathcal{L}_{k+1} - \nabla\mathcal{L}_k \quad (11)$$

A requirement for the existence of a solution is the so-called curvature condition $\mathbf{s}_k^T\mathbf{y}_k > 0$, which ensures that the Hessian is positive definite and therefore invertible. This can be ensured by using a step size algorithm that is based on the Wolfe conditions,³¹ for example. Note that the vectors in equations 9 to 11 are not necessarily one-dimensional objects. As discussed later, in our use case we treat unitary matrices as abstract vectors with the corresponding Frobenius product serving as inner product.

L-BFGS³⁸ is an approximation of BFGS, designed specifically for high-dimensional problems. While BFGS stores \mathbf{B} explicitly, the limited memory version L-BFGS³⁸ approximates equation (9) iteratively, therefore only retaining vectors \mathbf{y} and \mathbf{s} from a fixed number of previous iterations (memory). In our case, \mathbf{y} and \mathbf{s} are matrices of size $n \times n$, making \mathbf{B} of size n^4 . This large scaling restricts BFGS to small systems, while L-BFGS is usually the method of choice for large-scale problems with a high-dimensional parameter space. With increasing memory size, the L-BFGS approximation approaches BFGS and if every step is stored they are mathematically equivalent.

When setting the memory size to 1, L-BFGS is closely related to CG methods, which also memorize the gradient at the previous point to update the search direction.³¹

After finding a search direction applying one of the above methods, a suitable step size has to be selected to determine an exact point along that path. Step size algorithms are in general independent of the way search directions are selected, although some are more suitable than others. Abrudan et al. suggest interpolating along the search path and calculating the maximum (minimum) of the resulting polynomial²⁸ to obtain a reasonable estimate.

3.1.2 Riemannian Geometry

A very elegant way to impose constraints on parameters is to exploit topological properties of the parameters. For a more detailed treatment of the concepts in this chapter, especially in the context of optimization, consider the references.^{28,30,39}

We introduce Riemannian manifolds, smooth manifolds equipped with a metric. In general, a smooth manifold \mathcal{M} is a topological space that fulfills special requirements regarding distance, neighborhood and differentiability. To each point $\mathbf{U} \in \mathcal{M}$, a tangent space $T_{\mathbf{U}}\mathcal{M}$ is attached, i.e., the set of all possible tangent vectors at that point.

Consider a smooth curve

$$\gamma(t) : \mathbb{R} \rightarrow \mathcal{M}, \quad \gamma(0) = \mathbf{U}. \quad (12)$$

If \mathcal{M} is a submanifold of Euclidean space, a tangent vector \mathbf{X} to \mathcal{M} at point \mathbf{U} is intuitively defined as the derivative of this curve at $t = 0$,

$$\mathbf{X}_{\mathbf{U}} \equiv \left. \frac{d}{dt} \gamma(t) \right|_{t=0} \quad (13)$$

In this sense, a tangent vector defines the direction of a curve on the manifold.

A textbook example for a mapping procedure between tangent spaces and the manifold itself is the exponential map (see Eq.(16)), which enables movement along curves.

Riemannian manifolds are equipped with a Riemannian metric, defined on each tangent space as inner product $g(\mathbf{X}, \mathbf{Y}) = \langle \mathbf{X}, \mathbf{Y} \rangle$, where \mathbf{X}, \mathbf{Y} are tangent vectors.

3.1.3 The unitary group $U(n)$

A key property of unitary $n \times n$ matrices is that they form a Lie group $U(n)$, with matrix multiplication as a group action. The tangent space of the point at unity is highlighted as the Lie algebra of the group, $T_{\mathbf{I}}U(n) \equiv \mathfrak{u}(n)$, consisting of all skew-hermitian $n \times n$ matrices.

The group action defines two maps, known as *right translation* and *left translation*, meaning the multiplication of a point $\mathbf{V} \in U(n)$ by another point on the right:

$$\begin{aligned} R_U : U(n) &\rightarrow U(n) \\ \mathbf{V} &\mapsto \mathbf{V}U \equiv \mathbf{V}' \end{aligned} \quad (14)$$

and equivalently for left translation.

A tangent vector $\mathbf{X}_{\mathbf{V}} \in T_{\mathbf{V}}U(n)$ can be translated in the same way to another tangent space $T_{\mathbf{V}' }U(n)$:

$$\begin{aligned} R_{U*} : T_{\mathbf{V}}U(n) &\rightarrow T_{\mathbf{V}' }U(n) \\ \mathbf{X}_{\mathbf{V}} &\mapsto \mathbf{X}_{\mathbf{V}}U \equiv \mathbf{X}_{\mathbf{V}'} \end{aligned} \quad (15)$$

Importantly, these translations are isometries with respect to the Riemannian metric, so distances are preserved, allowing for the simple movement of curves and tangent vectors between points on the manifold. Following equation 15, every vector in the Lie algebra

$X_I \in \mathfrak{u}$ can be moved to any tangent space $T_U U(n)$ by multiplication with U from the right, $X_U = X_I U$, and vice versa every tangent vector can be easily translated to the Lie algebra: $X_I = X_U U^\dagger$. This makes the Lie algebra a very convenient choice for calculations involving multiple tangent vectors.

The exponential mapping $\exp : \mathfrak{u} \rightarrow U(n)$ maps an element $\mathbf{X} \in \mathfrak{u}$ to the group, given by the matrix exponential

$$\exp(\alpha \mathbf{X}) = \gamma(\alpha), \quad (16)$$

where the curve $\gamma : \mathbb{R} \rightarrow U(n)$ is a parameterized geodesic, the shortest path between two points of the group. This can be understood as taking a direction \mathbf{X} and moving along the corresponding geodesic curve.

The concepts in this chapter are also valid for the orthogonal group $O(n)$, consisting of orthogonal matrices as elements, while skew-symmetric matrices form the Lie algebra.

3.1.4 Optimization on the Unitary Group

Combining the previously discussed ideas, optimization algorithms originally designed as unconstrained in the Euclidean parameter space can be generalized to Riemannian manifolds. Equipped with the Frobenius inner product as Riemannian metric, $g(\mathbf{X}, \mathbf{Y}) = \text{Tr}(\mathbf{X}^\dagger \mathbf{Y})$, the unitary group $U(n)$ forms a Riemannian manifold.

According to Abrudan et al.,²⁷ the gradient of a function $\mathcal{L} : U(n) \rightarrow \mathbb{R}$ at some point $U \in U(n)$ is given by

$$\nabla \mathcal{L}(U) = \mathbf{\Gamma} - U \mathbf{\Gamma}^\dagger U \quad (17)$$

where $\mathbf{\Gamma} \equiv d\mathcal{L}/du_{ij}$. Subsequently, this gradient is translated to the Lie algebra via right translation:

$$\mathbf{G}(U) \equiv \nabla \mathcal{L}(U) U^\dagger = \mathbf{\Gamma} U^\dagger - U \mathbf{\Gamma}^\dagger \quad (18)$$

The algorithms SA, CG and BFGS are now introduced following section 3.1.1, utilizing the translated gradient $\mathbf{G}(U)$ to obtain the search direction \mathbf{H}_k . This vector is mapped to

the group using the exponential map in equation (16), the emanating curve $\exp(\alpha \mathbf{H}_k)$ is transported to \mathbf{U}_k to obtain \mathbf{U}_{k+1} :

$$\mathbf{U}_{k+1} = \exp(\alpha \mathbf{H}) \mathbf{U}_k \quad (19)$$

where the scaling factor α serves as step size.

In the case of L-BFGS, the fact that $U(n)$ is a Lie group is especially advantageous. Vectors y_i and s_i do not need to be transported to the new iterate to calculate the search direction, as calculations can be performed in the Lie algebra.

3.2 Implementation

The CG and SA solvers are implemented in the publicly available Julia package `Lucon.jl` (Loss optimization under unitary constraint)²⁴ as well as in VASP.⁹ The implementation of the L-BFGS solver is currently available in a development version of VASP. Pseudocode for this algorithm is shown in Alg. 1, following the work of Huang et al. and Nocedal et al.^{29,31} The two-loop recursion was developed by Nocedal et al.³¹ and efficiently computes the L-BFGS search direction. For step size calculations, we utilize the method developed by Abrudan et al.²⁸ To validate our implementation and confirm our results, we repeated all calculations using the `manopt.jl` package by Bergmann et al.,^{40,41} where we selected a step size algorithm based on the Hager-Zhang scheme.^{42,43} The Euclidean derivative for the IBOs reads

$$\begin{aligned} \Gamma_{ij}^{\text{PM}} &= \frac{\partial \mathcal{L}^{\text{PM}}}{\partial u_{ij}^*} \\ &= 2 \sum_A^{N_{\text{atoms}}} \sum_k^{N_{\text{occ}}} \langle \chi_i | \mathbf{P}_A | \chi_k \rangle u_{kj} \left| \sum_{lm}^{N_{\text{occ}}} \langle \chi_l | \mathbf{P}_A | \chi_m \rangle u_{lj}^* u_{mj} \right|. \end{aligned} \quad (20)$$

Algorithm 1 L-BFGS algorithm implementation

```
choose memory size  $m$ , break condition  $\epsilon$ 
choose starting point  $U_0$ 
calculate the initial gradient  $G(U_0)$  from equation (18)
 $s_i, y_i, \rho_i \leftarrow 0$ 
 $\lambda \leftarrow 1$ 
 $k \leftarrow 0$ 
repeat
   $k \leftarrow k + 1$ 
  procedure TWO-LOOP RECURSION
     $q \leftarrow G(U_k)$ 
    for  $i = m, m - 1, \dots, 1$  do
       $a_i \leftarrow \rho_i g(s_i, q)$ 
       $q \leftarrow q - a_i y_i$ 
    end for
     $r \leftarrow \lambda q$ 
    for  $i = 1, \dots, m$  do
       $b \leftarrow \rho_i g(y_i, r)$ 
       $r \leftarrow r + s_i(a_i - b)$ 
    end for
     $H_k \leftarrow -r$ 
  end procedure
  perform step size algorithm to obtain  $\alpha_k$ 
   $U_{k+1} = \exp(\alpha_k H_k) U_k$ 
  calculate  $G(U_{k+1})$ 
  for  $i = 1, \dots, m - 1$  do
     $s_i \leftarrow s_{i+1}, \quad y_i \leftarrow y_{i+1}, \quad \rho_i \leftarrow \rho_{i+1},$ 
  end for
   $s_m \leftarrow \alpha_k H_k$ 
   $y_m \leftarrow G(U_{k+1}) - G(U_k)$ 
   $\rho_m \leftarrow 1/g(s_m, y_m)$ 
   $\lambda \leftarrow g(s_m, y_m)/g(y_m, y_m)$ 
until  $\|G(U_k)\| < \epsilon$ 
```

3.3 Results

We performed computations for several molecules, molecular crystals, bulk solids and systems with broken translational symmetry. A special focus was on large supercells. If not stated otherwise, the calculations were initialized with random unitary matrices and a break condition for the gradient norm of $\|\mathbf{G}\| = \sqrt{\langle \mathbf{G}, \mathbf{G} \rangle} < 10^{-5}$ was chosen as the convergence

criterion. We measure the *performance* of an algorithm by the number of iterations required to reach convergence.

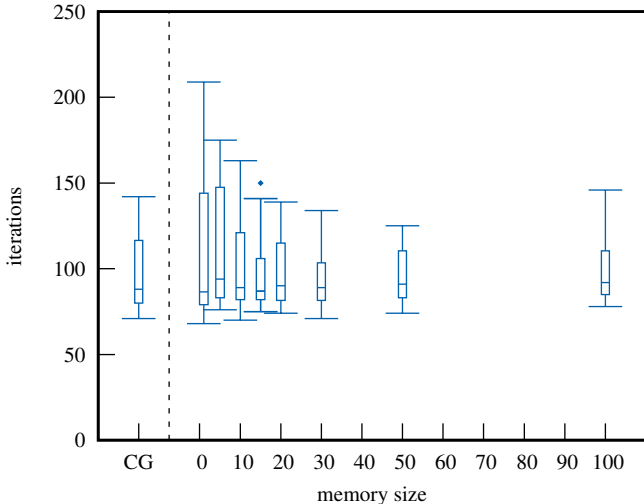


Figure 1: Box-and-whisker plot of the number of required iterations against the number of memorized L-BFGS steps compared to CG for a graphene supercell (162 atoms) with flower defects.

Surprisingly, specifically for periodic systems, large L-BFGS memory sizes do not necessarily lead to improved performance for IBO localization, as shown in Fig.1 for a graphene flower defect system (supercell with 324 occupied orbitals). However, the statistical variance of the required number of iterations decreases with higher memory, while the increase in computational cost is negligible. If not stated otherwise, a fixed memory size of 20 is used for our L-BFGS calculations. Note that the performance of CG and L-BFGS is similar for this example, an observation that is consistent across all periodic systems tested.

Fig. 2 shows the median number of necessary iterations against the system size for a selected set of systems using the L-BFGS solver. The scaling of the iterations with system size is roughly proportional to the fourth root of the number of occupied orbitals n , i.e. sublinear, illustrated by the dashed lines.

In Tab. 1, the median number of required iterations are listed for L-BFGS, CG and SA algorithms. Interestingly, for supercells with broken symmetry, L-BFGS and CG show a performance similar to that for the pristine case, as the results indicate for the flower

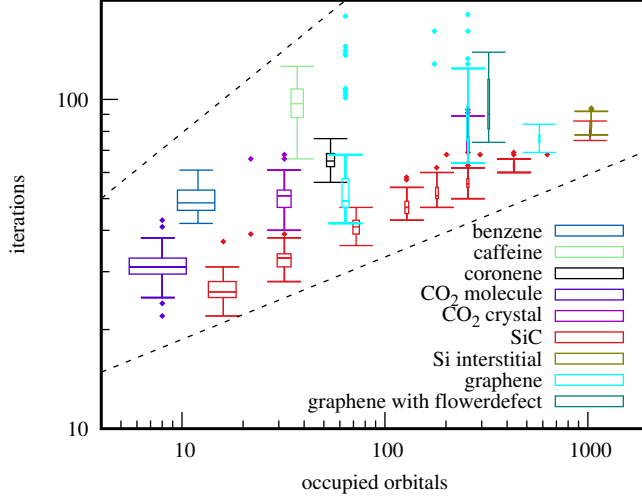


Figure 2: Box-and-whisker plot of the L-BFGS iterations against occupied orbitals n for several systems and supercell sizes. The dashed lines are proportional to \sqrt{n} and $n^{1/4}$ respectively, giving an idea of scaling.

Table 1: Median number of required iterations for L-BFGS, CG and SA solvers for several systems of various cell size (number of occupied orbitals).

material / molecule	#occ	L-BFGS	CG	SA
benzene	12	49	83	7093
caffeine	37	97	132	3217
coronene	54	65	85	671
CO ₂ molecule	8	31	38	171
CO ₂ crystal	32	51	53	269
SiC	256	73	81	316
	16	26	26	54
	32	33	33	68
	72	41	41	87
	128	47	45	102
	180	51	50	110
defect Si	256	56	53	120
	432	63	58	134
	1040	84	74	154
	64	50	51	124
graphene	256	89	78	197
	576	76	67	155
	324	90	88	265
flower defect graphene	324	90	88	265

defect graphene and Si with interstitial defects. L-BFGS and CG outperform SA for all test systems, L-BFGS has an advantage over CG only for molecules.

Table 2: For several graphene supercells, the algorithms not always converge to the same value of the cost function. The percentage of runs (out of 60 each) converging to the respective maximum is given in brackets. Notably, when converging to a lower value, the number of iterations is considerably higher. These outliers are also visible in Fig. 2 for the graphene cells.

material	#occ	largest maximum		second largest maximum	
		iterations	cost per #occ	iterations	cost per #occ
graphene	64	49 (92%)	1.1357	112 (8%)	1.1278
	256	87 (90%)	1.1346	126 (7%)	1.1293
	576	76 (100%)	1.1430	0 (0%)	
flower defect	324	83 (62%)	1.1350	119 (38%)	1.1341

Notably, some graphene cells exhibit outliers with a substantially higher number of iterations, approaching other local extrema. This behavior, visible in Fig. 2, is further quantified in Tab. 2 for the L-BFGS algorithm. For example, flower defect graphene calculations (324 occupied orbitals) converge to a slightly worse maximum in 38% of runs. Similar observations were made with the manopt.jl package considering CG and L-BFGS, using a different line search method.

Table 3: Comparison of the the average number of necessary iterations for metal oxides and a set of other materials employing the intrinsic bond orbital (IBO), Foster-Boys (FB), and von-Niessen (VN) localization functionals. Supercells containing a comparable number of occupied orbitals were considered. The average was calculated from 4 runs initialized with random unitary matrices.

material	oxide	#occ	IBO	FB	VN
SiC	non-oxide	256	53	140	39
CO ₂	molecular oxide crystal	256	81	546	294
SiO ₂	non-metal oxide	288	155	496	154
TiO ₂	metal oxide	288	678	1628	605
MgO	metal oxide	288	1737	1464	365

As listed in Tab. 3, metal oxides require about one order of magnitude more iterations for a fixed convergence threshold than other systems. Here, all considered localization functionals IBO, FB and VN show a similar trend. The slow and erratic decrease of the gradient

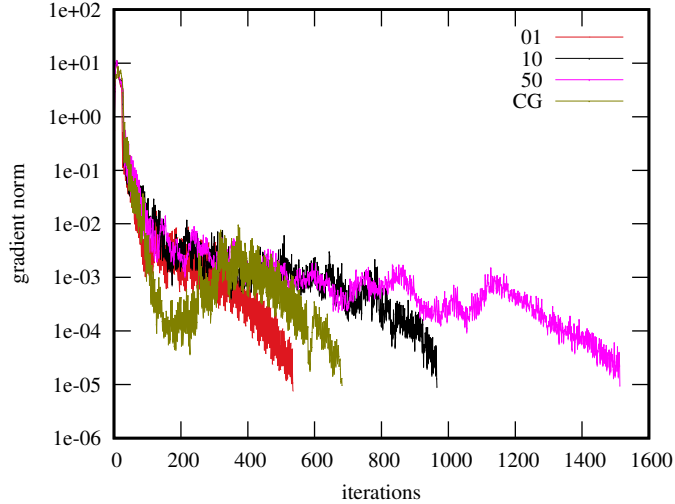


Figure 3: Convergence of L-BFGS with several memory size settings and CG, for a TiO_2 supercell (72 atoms, 288 occupied orbitals), the unity matrix serves as starting point (i.e. starting from bloch orbitals).

norm can be seen in Fig. 3 for a TiO_2 supercell (72 atoms, 288 occupied orbitals).

In contrast, a typical convergence pattern of non-oxides is shown in Fig. 4 using the aforementioned graphene flower defect supercell as an example. From a certain iteration step onwards (in this case somewhere between 50 and 60 iterations), convergence is consistently exponential.

The largely cubic scaling of the L-BFGS runtime per iteration and the system size is depicted in Fig. 5 for SiC. Except for very small cells, where the impact of several inexpensive routines is visible, the runtime scales proportionally to n^3 , where n is the number of occupied orbitals. This behavior is expected, as n determines the size of most of the involved matrices and consequently the cost of matrix operations. CG and SA are only marginally faster, on average by 3.5% and 4.1%, respectively, disregarding the two smallest cells. It can be stated that the additional complexity of L-BFGS is insignificant in relation to the cost of other routines like gradient calculation or line search algorithm.

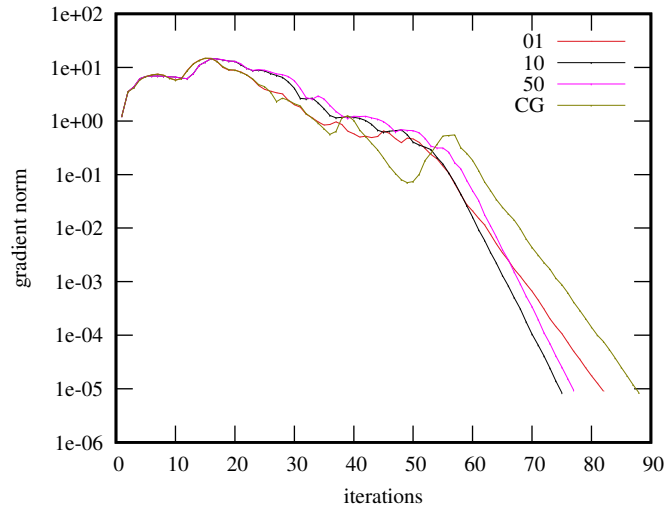


Figure 4: Convergence of L-BFGS with several memory size settings and CG, for a graphene supercell (162 atoms) with flower defects, the unity matrix serves as starting point (i.e. starting from bloch orbitals).

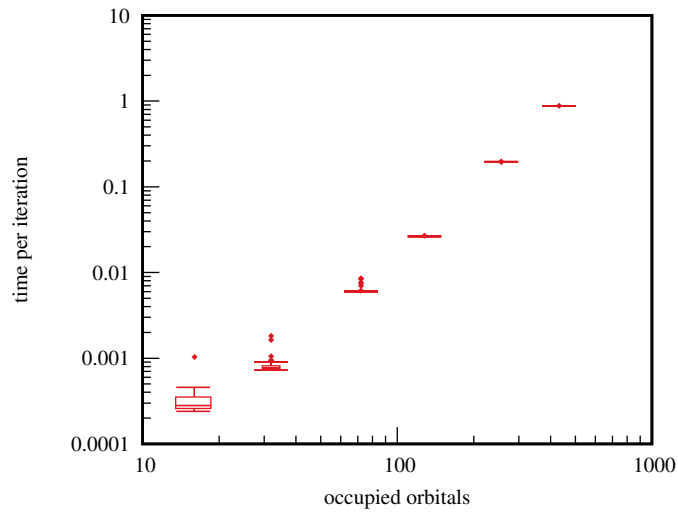


Figure 5: L-BFGS runtime per iteration in seconds against occupied orbitals, n , of SiC supercells, showing a n^3 scaling.

A Comment on the DIIS Technique

We implemented a Direct Inversion in the Iterative Subspace (DIIS) technique to investigate its potential for accelerating convergence to the optimum. Our implementation was modeled after the documentation by C. D. Sherrill.⁴⁴ Essentially, the DIIS technique is a mixer that seeks to find optimal linear combinations of previous iteration steps. This technique is well-established for accelerating iterative solvers in finding the HF ground state. When finding an optimal unitary matrix, this matrix must be parametrized to construct linear combinations of previous solutions, resulting in a new unitary matrix. While several parametrizations exist,⁴⁵ we used the exponential parametrization.

We applied the DIIS technique on top of our discussed solvers, which generate the trial vectors and residuals for DIIS. The number of trial vectors and residuals was tested in the range of 5 to 20. Additionally, a threshold for the gradient norm was set and tested within the range of 10^{-1} to 10^{-4} to ensure the DIIS solver did not start before the gradient norm fell below this threshold.

Although our DIIS implementation outperformed the SA solver, it did not demonstrate any advantage over the CG or BFGS solvers with our settings. While we cannot conclusively state that no effective DIIS implementation exists for accelerating convergence, we did not pursue this approach further due to our negative results.

3.4 Discussion

In this first part of the paper, we consider the performance of various solvers, avoiding any bias such as initial guesses. In contrast to previous studies by Clement et al.,¹⁸ we cannot confirm a significant advantage of L-BFGS over CG for any of the materials examined. Both methods are substantially more efficient than the SA, each in their respective Riemannian version. The similar performance of CG and L-BFGS, and the latter's weak dependence on memory size, demonstrates the challenges associated with the L-BFGS Hessian approximation especially in the context of IBO localization. In FB localization, for example, larger

L-BFGS memory has a positive effect, and L-BFGS performance is superior to CG.

L-BFGS iterations are only marginally slower than CG and SA in runtime measurements, dispelling a potential disadvantage and indicating the runtime dominance of other routines like gradient calculation or step size search. Runtime per iteration scales cubically with the number of occupied orbitals.

For several graphene supercells, a certain percentage of runs approach slightly different maxima, a behavior that is persistent for all tested solvers.

We find that some metal oxides converge significantly slower than other test systems and speculate that this issue is due to the ionic character of the material. The localized orbitals exhibit similar shape as atomic orbitals and superpositions of these atomic-like orbitals leave the cost function almost untouched. This adds to the potential problem of local extrema and saddle points, which are very common for high dimensional cost functions.

These challenges highlight the necessity for improvements such as good initial guesses or even better solvers, also the development of new localization functionals should be considered.

Note, that comparison with other works which model solids via small primitive cells and \mathbf{k} -point sampling^{18,20,46} should be taken with care, as we employ a supercell formulation using a single \mathbf{k} -point, the Γ -point, for sampling the Brillouin Zone (BZ) due to our focus on material models with large cells and broken translational symmetry.

4 Properties of Intrinsic Bond Orbitals

In the second main part of the paper, we investigate spatial properties of IBOs for a variety of insulating solids, as listed in Tab. 4. These IBOs were constructed from Hartree-Fock (HF) orbitals, and their spatial character were analyzed in relation to the material's crystal structure and band gap. A focus was the average orbital spread of the IBOs and its relationship with geometric properties, specifically the nearest neighbor distance (d_{NN}) and the number of nearest neighbors ($\# \text{NN}$). Our findings reveal that the orbital spread of the

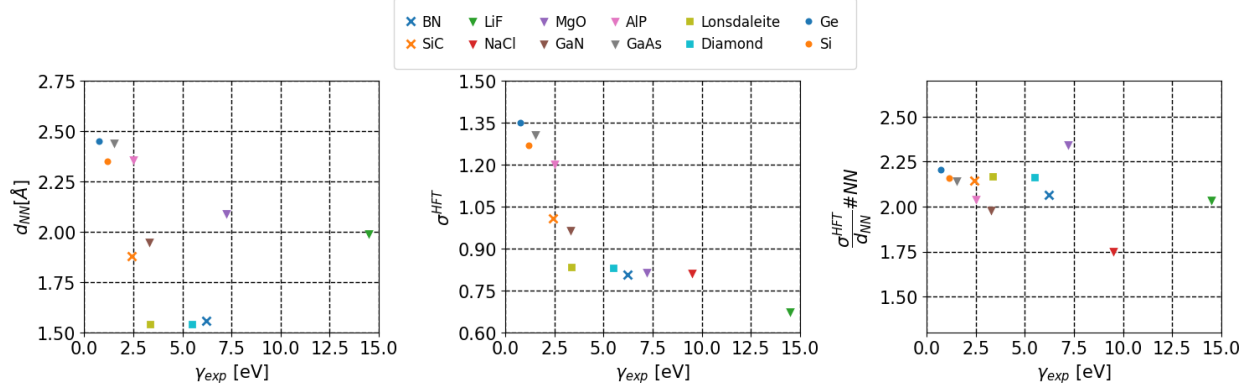


Figure 6: Plot of the nearest neighbor distance d_{NN} (left), the IBO orbital spread σ_{HF} (centre), and relation between orbitals spread and $d_{\text{NN}}/\#\text{NN}$ (right) plotted against the experimental band gap of all considered materials.

valence electrons per nearest neighbor distance, multiplied by the number of nearest neighbors, remains relatively stable across the materials considered. This can be captured by the empirical relation $\sigma_{\text{HF}} \approx 2.1\alpha$, where $\alpha = \frac{d_{\text{NN}}}{\#\text{NN}}$. This trend was consistent across various crystal structures, independent of the band gap, providing a useful estimate for predicting the spatial extent of localized orbitals (see Fig. 6).

Table 4: List of considered materials in Sec. 4. The structure column refers to the Strukturbericht designation. Mixed bonds have ionic and covalent character. The lattice constant a , the nearest neighbor distance d_{NN} , the number of nearest neighbors $\#\text{NN}$, the IBO orbital spread σ_{HF} , and the experimental band gap γ_{exp} are also provided.

	structure	bond	$a[\text{\AA}]$	$d_{\text{NN}}[\text{\AA}]$	$\#\text{NN}$	$\sigma_{\text{HF}}[\text{\AA}]$	$\gamma_{\text{exp}}[\text{eV}]$
C (Diamond)	A4	covalent	3.57	1.54	4	0.832	5.48
Si	A4	covalent	5.431	2.35	4	1.268	1.17
Ge	A4	covalent	5.652	2.45	4	1.351	0.74
NaCl	B1	ionic	5.569	2.78	6	0.813	9.50
MgO	B1	ionic	4.189	2.09	6	0.817	7.22
LiF	B1	ionic	3.972	1.99	6	0.676	14.5
SiC	B3	mixed	4.346	1.88	4	1.009	2.42
BN	B3	mixed	3.592	1.56	4	0.806	6.22
AlP	B3	ionic	5.451	2.36	4	1.204	2.51
GaAs	B3	ionic	5.64	2.44	4	1.307	1.52
GaN	B3	ionic	4.509	1.95	4	0.966	3.30
C (Lonsdaleite)	B4	covalent	4.347	1.54	4	0.835	3.35

We also analyzed the decay of the Fock exchange matrix entries,

$$K_{ij} = -\frac{1}{2} \int d^3r_1 \int d^3r_2 \frac{\mathcal{W}_i^*(\mathbf{r}_1)\mathcal{W}_j(\mathbf{r}_1) \mathcal{W}_j^*(\mathbf{r}_2)\mathcal{W}_i(\mathbf{r}_2)}{|\mathbf{r}_1 - \mathbf{r}_2|}, \quad (21)$$

in the basis of Wannier orbitals $\mathcal{W}_i(\mathbf{r})$ (IBOs). Two truncation methods were employed to estimate the error per atom when truncating these matrix entries. This error is defined as

$$\varepsilon = \left| \sum_{ij} K_{ij} - \sum_{ij}^{\text{trunc.}} K_{ij} \right| / N_A, \quad (22)$$

where N_A is the number of atoms. Truncation method 1 involves zeroing out matrix elements below a certain threshold (Fig. 7), while Method 2 uses a cutoff radius based on the distance between Wannier orbitals (Fig. 8). It is striking that no significant difference can be observed between germanium and diamond, for example. Note that germanium is a small-gap material with an experimental band gap of 0.74 eV, a high relative permittivity compared to diamond (which has a band gap of 3.35 eV), and is significantly less polarizable.

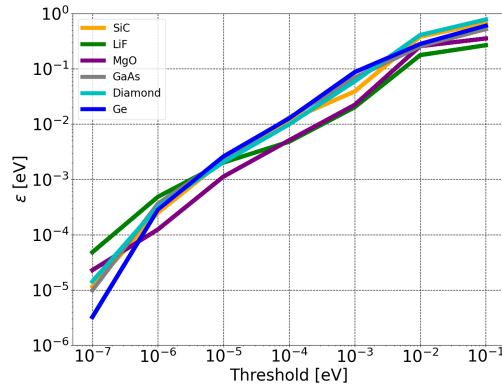


Figure 7: Error per atom ε for different thresholds of the exchange matrix entries using the truncation method 1 (see text for explanation).

Our findings on the truncation of the Fock exchange matrix further support the potential for computational savings due to its sparsity. This holds for both large-gap and small-gap materials, suggesting that the band gap has a relatively minor effect on the decay of matrix elements for practical purposes. Figure 9 shows the number of remaining non-zero Fock

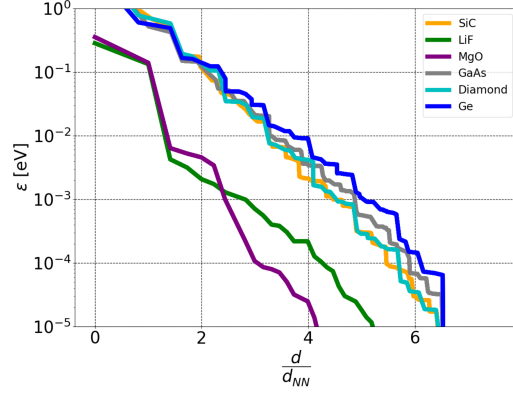


Figure 8: Error per atom with respect to the largest distance between the Wannier orbitals d_{\max} per nearest neighbour distance, using the truncation method 2 (see text for explanation)

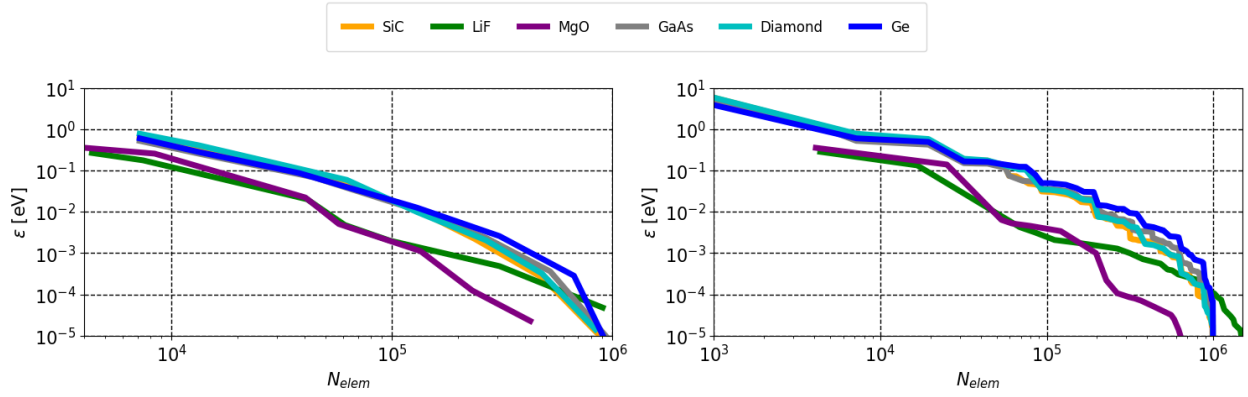


Figure 9: Fock exchange energy error per atom ε with respect to the number of non-zero elements N_{elem} of the Fock matrix using the truncation method 1 (left) and 2 (right), as explained in the text.

exchange matrix elements in dependence of ε for both methods.

In summary, the analysis of IBO properties across various materials reveals a correlation between orbital spread and geometric factors. This relationship provides a straightforward way to estimate the spatial extent of localized orbitals, which is crucial for the development of reduced-cost methods. Additionally, the truncation of the Fock exchange matrix demonstrates significant potential for reducing computational costs in large-scale simulations, with manageable errors across a wide range of materials.

5 Conclusion

In this work we studied the numerical construction and spatial properties of IBOs based on HF orbitals for a set of insulating solids. We reported a relation between the orbital spread measured in units of the nearest neighbor distance and the number of nearest neighbors. Independent of the band gap, this relation is relatively stable for all considered 3D semiconductors. It suggests that local methods based on the sparsity of Coulomb integrals can also be applied to materials with small band gaps without losing the sparsity. We verified this hypothesis for the particular case of the sparsity of the Fock exchange matrix in the basis of IBOs. Whether this can be extended to metallic solids or scenarios involving localized unoccupied orbitals, essential for many-electron correlation methods, remains an open question. This warrants further investigation in future work.

Additionally, we benchmarked various solvers to optimize the unitary matrix that transforms delocalized Bloch orbitals into localized Wannier orbitals, specifically in the form of IBOs. Our focus was on large simulation cells, which are crucial for realistic models, such as those involving surface phenomena and defects. Contrary to some previous studies, we did not observe a clear performance advantage of the L-BFGS solver, instead finding that both the CG and L-BFGS solvers exhibited similar performance. When using stochastic (unbiased) starting points, we found that constructing localized orbitals in supercells of metal

oxides pose a significant challenge, requiring an order of magnitude more iteration steps than for the other materials considered. This emphasizes the importance of well-chosen starting points and the potential value of non-iterative methods for constructing localized Wannier orbitals in solids.

Acknowledgements

T.S. acknowledges support from the Austrian Science Fund (FWF) [10.55776/ESP335]. The computational results presented have been achieved in part using the Vienna Scientific Cluster (VSC).

References

- (1) Edmiston, C.; Ruedenberg, K. Localized Atomic and Molecular Orbitals. *Reviews of Modern Physics* **1963**, *35*, 457–464.
- (2) Knizia, G. Intrinsic Atomic Orbitals: An Unbiased Bridge between Quantum Theory and Chemical Concepts. *Journal of Chemical Theory and Computation* **2013**, *9*, 4834–4843.
- (3) Knizia, G.; Klein, J. E. Electron Flow in Reaction Mechanisms—Revealed from First Principles. *Angewandte Chemie International Edition* **2015**, *54*, 5518–5522.
- (4) Engel, M.; Marsman, M.; Franchini, C.; Kresse, G. Electron-phonon interactions using the projector augmented-wave method and Wannier functions. *Physical Review B* **2020**, *101*, 184302.
- (5) Voloshina, E.; Usvyat, D.; Schütz, M.; Dedkov, Y.; Paulus, B. On the physisorption of water on graphene : a CCSD(T) study. *Physical Chemistry Chemical Physics* **2011**, *13*, 12041–12047.

- (6) Usvyat, D.; Maschio, L.; Schütz, M. Periodic and fragment models based on the local correlation approach. *WIREs Computational Molecular Science* **2018**, *8*, 1–27.
- (7) Kubas, A.; Berger, D.; Oberhofer, H.; Maganas, D.; Reuter, K.; Neese, F. Surface Adsorption Energetics Studied with “Gold Standard” Wave-Function-Based Ab Initio Methods: Small-Molecule Binding to TiO₂ (110). *The Journal of Physical Chemistry Letters* **2016**, *7*, 4207–4212.
- (8) Schäfer, T.; Libisch, F.; Kresse, G.; Grüneis, A. Local embedding of coupled cluster theory into the random phase approximation using plane waves. *The Journal of Chemical Physics* **2021**, *154*, 011101.
- (9) Schäfer, T.; Gallo, A.; Irmeler, A.; Hummel, F.; Grüneis, A. Surface science using coupled cluster theory via local Wannier functions and in-RPA-embedding: The case of water on graphitic carbon nitride. *The Journal of Chemical Physics* **2021**, *155*, 244103.
- (10) Lau, B. T. G.; Knizia, G.; Berkelbach, T. C. Regional Embedding Enables High-Level Quantum Chemistry for Surface Science. *The Journal of Physical Chemistry Letters* **2021**, *12*, 1104–1109.
- (11) Ye, H.-Z.; Berkelbach, T. C. Adsorption and Vibrational Spectroscopy of CO on the Surface of MgO from Periodic Local Coupled-Cluster Theory. *Faraday Discussions* **2024**,
- (12) Foster, J. M.; Boys, S. F. Canonical Configurational Interaction Procedure. *Reviews of Modern Physics* **1960**, *32*, 300.
- (13) von Niessen, W. Density localization of atomic and molecular orbitals - III. Heteronuclear diatomic and polyatomic molecules. *Theoretica Chimica Acta* **1973**, *29*, 29–48.
- (14) Pipek, J.; Mezey, P. G. A fast intrinsic localization procedure applicable for a b i n i t i o and semiempirical linear combination of atomic orbital wave functions. *The Journal of Chemical Physics* **1989**, *90*, 4916–4926.

- (15) Zicovich-Wilson, C. M.; Dovesi, R.; Saunders, V. R. A general method to obtain well localized Wannier functions for composite energy bands in linear combination of atomic orbital periodic calculations. *The Journal of Chemical Physics* **2001**, *115*, 9708–9719.
- (16) Marzari, N.; Mostofi, A. A.; Yates, J. R.; Souza, I.; Vanderbilt, D. Maximally localized Wannier functions: Theory and applications. *Reviews of Modern Physics* **2012**, *84*, 1419–1475.
- (17) Jónsson, E. O.; Lehtola, S.; Puska, M.; Jónsson, H. Theory and Applications of Generalized Pipek–Mezey Wannier Functions. *Journal of Chemical Theory and Computation* **2017**, *13*, 460–474.
- (18) Clement, M. C.; Wang, X.; Valeev, E. F. Robust Pipek–Mezey orbital localization in periodic solids. *Journal of Chemical Theory and Computation* **2021**, *17*, 7406–7415.
- (19) Ozaki, T. Closest Wannier functions to a given set of localized orbitals. *Physical Review B* **2024**, *110*, 125115.
- (20) Zhu, A.; Tew, D. P. Wannier Function Localization Using Bloch Intrinsic Atomic Orbitals. *The Journal of Physical Chemistry A* **2024**,
- (21) Kresse, G.; Hafner, J. Ab initio molecular dynamics for liquid metals. *Physical Review B* **1993**, *47*, 558.
- (22) Kresse, G.; Furthmüller, J. Efficient iterative schemes for ab initio total-energy calculations using a plane-wave basis set. *Physical Review B* **1996**, *54*, 11169.
- (23) Kresse, G.; Furthmüller, J. Efficiency of ab-initio total energy calculations for metals and semiconductors using a plane-wave basis set. *Computational Materials Science* **1996**, *6*, 15–50.
- (24) Lucon.jl. github.com/toschaefer/Lucon.jl.

- (25) Luenberger, D. G. The Gradient Projection Method along Geodesics. *Management Science* **1972**, *18*, 620–631.
- (26) Gabay, D. Minimizing a differentiable function over a differential manifold. *Journal of Optimization Theory and Applications* **1982**, *37*, 177–219.
- (27) Abrudan, T. E.; Eriksson, J.; Koivunen, V. Steepest Descent Algorithms for Optimization Under Unitary Matrix Constraint. *IEEE Transactions on Signal Processing* **2008**, *56*, 1134–1147.
- (28) Abrudan, T.; Eriksson, J.; Koivunen, V. Conjugate gradient algorithm for optimization under unitary matrix constraint. *Signal Processing* **2009**, *89*, 1704–1714.
- (29) Huang, W.; Gallivan, K. A.; Absil, P.-A. A Broyden class of quasi-Newton methods for Riemannian optimization. *SIAM Journal on Optimization* **2015**, *25*, 1660–1685.
- (30) Huang, W. Optimization algorithms on Riemannian manifolds with applications. Ph.D. thesis, The Florida State University, 2013.
- (31) Nocedal, J.; Wright, S. J. *Numerical optimization*; Springer, 1999.
- (32) Polak, E.; Ribiere, G. Note sur la convergence de méthodes de directions conjuguées. *Revue française d'informatique et de recherche opérationnelle. Série rouge* **1969**, *3*, 35–43.
- (33) Polak, E. *Computational methods in optimization: a unified approach*; Academic press, 1971; Vol. 77.
- (34) Broyden, C. G. The convergence of a class of double-rank minimization algorithms 1. general considerations. *IMA Journal of Applied Mathematics* **1970**, *6*, 76–90.
- (35) Fletcher, R. A new approach to variable metric algorithms. *The computer journal* **1970**, *13*, 317–322.

- (36) Goldfarb, D. A family of variable-metric methods derived by variational means. *Mathematics of computation* **1970**, *24*, 23–26.
- (37) Shanno, D. F. Conditioning of quasi-Newton methods for function minimization. *Mathematics of computation* **1970**, *24*, 647–656.
- (38) Liu, D. C.; Nocedal, J. On the limited memory BFGS method for large scale optimization. *Mathematical programming* **1989**, *45*, 503–528.
- (39) Qi, C. Numerical optimization methods on Riemannian manifolds. Ph.D. thesis, The Florida State University, 2011.
- (40) Bergmann, R. Manopt.jl: Optimization on Manifolds in Julia. *Journal of Open Source Software* **2022**, *7*, 3866.
- (41) Axen, S. D.; Baran, M.; Bergmann, R.; Rzecki, K. Manifolds.Jl: An Extensible Julia Framework for Data Analysis on Manifolds. *ACM Transactions on Mathematical Software* **2023**, *49*.
- (42) Hager, W. W.; Zhang, H. A New Conjugate Gradient Method with Guaranteed Descent and an Efficient Line Search. *SIAM Journal on Optimization* **2005**, *16*, 170–192.
- (43) Baran, M. ImprovedHagerZhangLinesearch.jl. <https://github.com/mateuszbaran/ImprovedHagerZhangLinesearch.jl>, 2024.
- (44) Sherrill, C. D. Some comments on accelerating convergence of iterative sequences using direct inversion of iterative subspace (DIIS). *Acessado em http://vergil.chemistry.gatech.edu/notes/diis. Setembro* **2004**,
- (45) Shepard, R.; Brozell, S. R.; Gidofalvi, G. The Representation and Parametrization of Orthogonal Matrices. *Journal of Physical Chemistry A* **2015**, *119*, 7924–7939.
- (46) Lehtola, S.; Jónsson, H. Unitary optimization of localized molecular orbitals. *Journal of chemical theory and computation* **2013**, *9*, 5365–5372.

TOC Graphic

